Photonics-Based Broadband Microwave Instantaneous Frequency Measurement by Frequency-to-Phase-Slope Mapping

Jingzhan Shi, Fangzheng Zhang, *Member, IEEE*, De Ben, and Shilong Pan, *Senior Member, IEEE*

***Abstract*— A photonics-based broadband microwave instantaneous frequency measurement (IFM) method is proposed by monotonously mapping the frequency to the slope of the time-varying phase of the microwave signal under test. This frequency-to-phase-slope mapping approach is realized utilizing a variable photonic delay line and a microwave photonic in-phase/quadrature (I/Q) mixer, where the I/Q mixer is composed of two phase modulators connected tail to tail within a fiber loop, an optical 90° hybrid, and a pair of low-speed balanced photodiodes. Thanks to the monotonous frequency-to-phase-slope mapping property, as well as the use of photonic delay line and microwave photonic I/Q mixing, the IFM system can achieve a wide-range frequency measurement without ambiguity. An experiment is performed. The established IFM system is able to operate from 5 to 67 GHz with a measurement error of less than 500 MHz, which achieves the widest frequency measurement range ever recorded by photonics-based IFM systems. In addition, the influences of the I/Q phase mismatch and the amplitude noise on the performance of the IFM system are also discussed. We believe that this photonics-based IFM system is a promising solution for wideband microwave frequency measurements.**

***Index Terms*— Balanced photodetection, frequency measurement, microwave photonics, photonic in-phase/quadrature (I/Q) mixing, variable delay line (VDL).**

I. Introduction

INSTANTANEOUS frequency measurement (IFM) of an unknown microwave signal is critically important in radar, communication, and electronic warfare applications [1], [2]. Due to the broad spectral range in modern electronic applications, e.g., radars that carry out different functions typically operate within different frequency ranges, which can cover a bandwidth of tens of gigahertz [3], [4], an IFM system is required to estimate the frequency of unknown microwave signals over a large bandwidth. Currently, IFM is generally realized using electronic techniques [5], such as electrical delay-line-based IFM, digital IFM, and electrical filter-based IFM, which can achieve a high resolution but suffer from narrow operation bandwidth, high power consumption, and vulnerability to electromagnetic interference (EMI). In order to break the limitations confronted by electronic techniques, a variety of photonics-based approaches have been proposed for IFM, taking the advantage of photonic technologies such as broad bandwidth, low loss, and immunity to EMI [6]. Generally, the photonic-based IFM approaches can be classified into three categories, i.e., frequency-to-time mapping, frequency-to-space mapping, and frequency-to-power mapping [7], [8].

The frequency-to-time mapping can be realized into two schemes. In the first scheme, the frequency is mapped to a certain time delay utilizing a dispersive medium [9]. In this scheme, the frequency measurement range and resolution are limited by the speed of the optical ON–OFF switching and the sampling rate of the oscilloscope. In the second scheme, the frequency-to-time mapping is implemented by a frequency shifting recirculating delay line loop and a narrowband optical filter realized by in-fiber stimulated Brillouin scattering (SBS) effect [10]. With a large number of circulations, a broad frequency measurement range can be achieved. However, it also leads to a significant latency.

The frequency-to-space mapping method maps different frequencies into different space channels by an optical upconversion-and-split topology, i.e., the microwave signal under test (SUT) is modulated on an optical carrier and then split into multiple channels by an optical channelizer. The frequency of the microwave signal can be figured out based on the output of each channel. The optical channelizer can be implemented by a Fabry–Perot etalon [11], [12], an arrayed-waveguide grating [13] or a diffraction grating [14]. The main drawback of this scheme is the poor measurement resolution originated from the optical channelizer. In addition, the system usually has a high cost and a high complexity, considering a large photodiode (PD) array is required.

The main idea of frequency-to-power mapping approach is to construct a relationship between the frequency of the SUT and the ratio of two different optical or microwave power functions, named as amplitude comparison function (ACF) [15]. A disadvantage of this kind of system is that it is hard to achieve a high-resolution measurement due to the small slope of the ACF at a certain frequency range. To solve

Manuscript received July 29, 2018; revised September 27, 2018; accepted September 28, 2018. Date of publication November 1, 2018; date of current version February 5, 2019. This work was supported in part by the Natural Science Foundation of Jiangsu Province under Grant SBK201803001, in part by the National Science Foundation of China Program under Grant 61871214 and Grant 6157820, in part by the Postgraduate Research and Practice Innovation Program of Jiangsu Province under Grant KYCX17_0289, and in part by the Fundamental Research Funds for the Central Universities under Grant NS2018028 and Grant NC2018005. This paper is an expanded version from the IEEE International Wireless Symposium, Chengdu, China, May 6–9, 2018. *(Corresponding authors: Fangzheng Zhang; Shilong Pan.)*

The authors are with the Key Laboratory of Radar Imaging and Microwave Photonics, Ministry of Education, Nanjing University of Aeronautics and Astronautics, Nanjing 210016, China (e-mail: zhangfangzheng@nuaa.edu.cn; pans@nuaa.edu.cn).

Color versions of one or more of the figures in this paper are available online at http://ieeexplore.ieee.org.

Digital Object Identifier 10.1109/TMTT.2018.2875683

this problem, IFMs with tunable measurement range and resolution have been reported by varying the wavelength of the laser sources [16]–[18] or using SBS effect [19]. Another possible solution to this problem is to generate an ACF with a large slope over a wide frequency range by comparing two complimentary frequency-to-power functions [20]–[24]. Despite all these efforts, a common problem severely limits the unambiguous frequency measurement range of the frequency-to-power mapping-based IFM method, i.e., the nonmonotonic ACF results in the frequency measurement ambiguity, which limits the upper bound of unambiguous frequency measurement range to the position of the first notch of the ACF.

Therefore, it remains a hot topic to explore methods that can achieve accurate frequency measurement in a broad bandwidth. In this paper, for the first time to the best of our knowledge, we propose an IFM method by monotonously mapping the frequency to the slope of a time-varying phase of the SUT, i.e., the frequency-to-phase-slope mapping method. In this method, the phase of the SUT is acquired by introducing a uniformly varying time delay between two replicas of the SUT and then performing a digital in-phase/quadrature (I/Q) phase demodulation. This IFM method is free from measurement ambiguity, and the operation bandwidth is only limited by the bandwidth of the devices applied in the system. To overcome the electronic bandwidth limitation and achieve a large frequency measurement range, a photonics-based IFM system is proposed based on the frequency-to-phase-slope mapping method, in which a variable photonic delay line and a microwave photonic I/Q mixer are incorporated. Previously, we have proposed several microwave photonic I/Q mixers by cascading a polarization modulator (PolM) with a phase modulator (PM) [25], cascading a Mach–Zehnder modulator (MZM) with a PolM [26], or cascading a PM with a parallel installed PM and MZM [27], which can realize wideband I/Q mixing. However, precise polarization control or MZM bias control is needed in these systems. In this paper, the microwave photonic I/Q mixer is realized based on an optical 90° hybrid followed by balanced photodetection, which is free from complex polarization control and bias control [28]. This paper is organized as follows. In Section II, the principle of the proposed IFM method and the photonics-based IFM system are described. In Section III, a proof-of-concept experiment is conducted. The frequency measurement resolution and bandwidth are demonstrated. In Section IV, the influences of the phase mismatch and the amplitude noise in the I/Q signals are discussed. In Section V, the conclusion is drawn.

II. Principle

A. Basic Principle

Fig. 1 shows the schematic of the proposed IFM method based on the frequency-to-phase-slope mapping. The SUT can be written as

$$v_{\mathrm{s}}(t) = V_0 \cos(2\pi f_{\mathrm{s}} t) \tag{1}$$

where V_0 is the amplitude and f_{s} is the frequency to be measured. The SUT is divided into two branches through a power divider. In the upper branch, a uniformly time-varying delay is introduced by adjusting a variable delay line (VDL) with a constant speed. The signal after the VDL can be expressed as

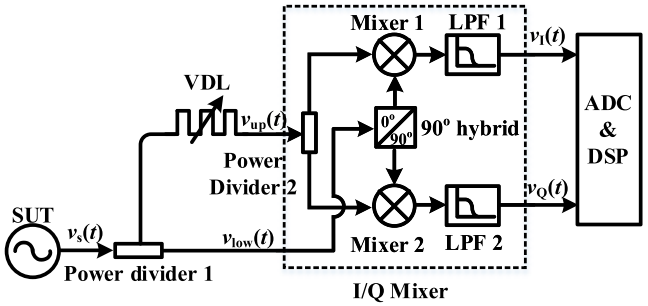

Fig. 1. Schematic of the proposed IFM method. SUT: signal under test, VDL: variable delay line, LPF: low-pass filter, ADC: analog-to-digital converter, and DSP: digital signal processing.

$$v_{\mathrm{up}}(t) = \frac{V_0}{\sqrt{2}} \cos[2\pi f_{\mathrm{s}}(t - \upsilon t)] \tag{2}$$

where υ is the varying speed of the time delay. The signal in the lower branch is

$$v_{\mathrm{low}}(t) = \frac{V_0}{\sqrt{2}} \cos(2\pi f_{\mathrm{s}} t). \tag{3}$$

Then, the signals in (2) and (3) are sent to an I/Q mixer, which consists of a power divider, a 90° hybrid, two mixers, and two low-pass filters. The voltages at the output of the I/Q mixer are written as

$$\begin{aligned} I(t) &= \frac{V_0^2}{8} \cos(2\pi f_{\mathrm{s}} \upsilon t) \\ Q(t) &= \frac{V_0^2}{8} \sin(2\pi f_{\mathrm{s}} \upsilon t). \end{aligned} \tag{4}$$

An analog-to-digital converter (ADC) is used to digitalize the output signals of the I/Q mixer. Here, the sampling rate of the ADC needs to be larger than $2 f_{\mathrm{s}} \upsilon$, which can be very small by choosing a low varying speed of the time delay. The digitalized signals are, then, sent to a computer for digital signal processing (DSP), where the following procedures are proceeded:

$$\begin{aligned} \phi(t) &= 2\pi f_{\mathrm{s}} \upsilon t = \arctan\left(\frac{Q(t)}{I(t)}\right) \\ f_{\mathrm{s}} &= \frac{k[\phi(t)]}{2\pi \upsilon} \end{aligned} \tag{5}$$

where $k[\phi(t)]$ denotes the slope of $\phi(t)$ with respect to time. It can be seen that the frequency to be measured is monotonically mapped to the slope of a calculated phase, which means that the frequency can be measured without ambiguity. As a result, the bandwidth limitation due to the ambiguity can be eliminated. However, the bandwidth is still limited by the electrical VDL and I/Q mixer in Fig. 1. In order to solve this problem, a photonic-assisted realization of the proposed IFM method is proposed, as demonstrated in Section III-B.

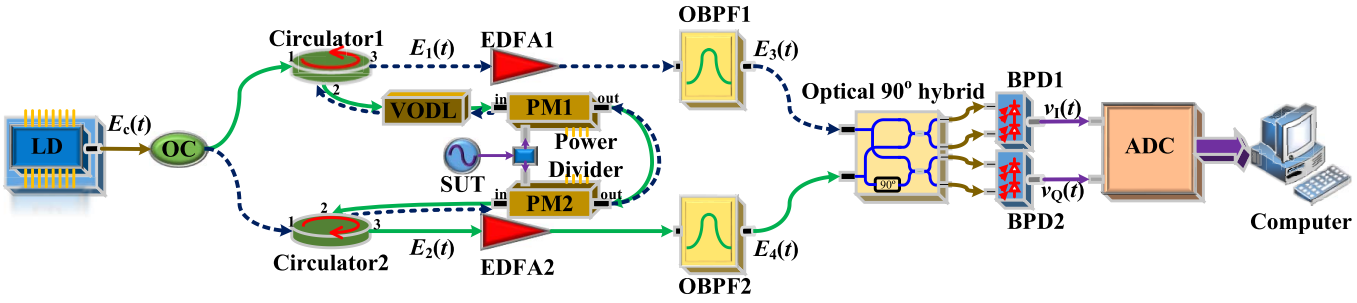

Fig. 2. IFM system based on VODL and photonic-assisted microwave I/Q mixer. LD: laser diode, OC: optical coupler, PM: phase modulator, VODL: variable optical delay line, EDFA: erbium-doped fiber amplifier, OBPF: optical bandpass filter, and BPD: balanced PD.

B. Photonics-Based IFM System

In order to overcome the possible bandwidth limitation due to the electrical components, a photonics-based IFM system based on the frequency-to-phase-slope mapping is proposed, where the electrical VDL and I/Q mixer are replaced by a variable optical delay line (VODL) and a microwave photonic I/Q mixer, respectively. The microwave photonic I/Q mixer is constructed applying two PMs, an optical 90° hybrid, and two low-speed balanced PDs (BPDs), as shown in Fig. 2, where the two PMs are connected tail to tail in a fiber loop. Compared with the schemes in [25]–[27], no special polarization control or bias control is needed, and better stability can be achieved.

In Fig. 2, the electrical field of the optical carrier generated by the laser diode can be written as

$$E_{\mathrm{c}}(t) = E_0 e^{j(2\pi f_{\mathrm{c}} t + \varphi_{\mathrm{c}}(t))} \tag{6}$$

where E_0, f_{c}, and $\varphi_{\mathrm{c}}(t)$ are the amplitude, frequency, and phase noise of the optical carrier, respectively. This optical carrier is injected into a loop comprising an optical coupler (OC), two circulators, a VODL, and two PMs, where the output port of PM1 is connected to the output port of PM2, and the two PMs are driven by two replicas of the SUT. The optical carrier is equally split into two branches by the OC. In one branch, the optical signal goes through the loop in the anticlockwise direction, as shown by the blue dashed line in Fig. 2. It should be noted that the PM is a traveling-wave modulator. When it is used in a reverse direction, the weak phase modulation can be ignored [29]. The optical carrier is phase modulated by PM2 and then delayed by the VODL. In this case, the time delay is introduced to both the optical carrier and the SUT. The electrical field of the optical signal at the third port of Circulator1 is

$$\begin{aligned} E_1(t) &\propto E_{\mathrm{c}}(t-\upsilon t)\, e^{j\beta_2 \cos[2\pi f_{\mathrm{s}}(t-\upsilon t)]} \\ &= E_0 e^{j\{2\pi f_{\mathrm{c}}(t-\upsilon t)+\varphi_{\mathrm{c}}(t-\upsilon t)+\beta_2\cos[2\pi f_{\mathrm{s}}(t-\upsilon t)]\}} \\ &\approx E_0 J_0(\beta_2)\, e^{j[2\pi f_{\mathrm{c}}(t-\upsilon t)+\varphi_{\mathrm{c}}(t-\upsilon t)]} \\ &\quad + E_0 J_1(\beta_2)\, e^{j\left[2\pi(f_{\mathrm{c}}+f_{\mathrm{s}})(t-\upsilon t)+\varphi_{\mathrm{c}}(t-\upsilon t)+\frac{\pi}{2}\right]} \\ &\quad + E_0 J_1(\beta_2)\, e^{j\left[2\pi(f_{\mathrm{c}}-f_{\mathrm{s}})(t-\upsilon t)+\varphi_{\mathrm{c}}(t-\upsilon t)+\frac{\pi}{2}\right]} \end{aligned} \tag{7}$$

where β_2 is the modulation index of PM2. In the other branch, the optical signal goes through the loop in the clockwise direction, as indicated by the green solid line. The optical signal is delayed by the VODL first and then phase modulated by PM1, which indicates that the time delay is only introduced into the optical carrier. The electrical field of the optical signal at the third port of Circulator2 is

$$\begin{aligned} E_2(t) &\propto E_{\mathrm{c}}(t-\upsilon t)e^{j\beta_1\cos(2\pi f_{\mathrm{s}}t)} \\ &= E_0 e^{j[2\pi f_{\mathrm{c}}(t-\upsilon t)+\varphi_{\mathrm{c}}(t-\upsilon t)+\beta_1\cos(2\pi f_{\mathrm{s}}t)]} \\ &\approx E_0 J_0(\beta_1) e^{j[2\pi f_{\mathrm{c}}(t-\upsilon t)+\varphi_{\mathrm{c}}(t-\upsilon t)]} \\ &\quad + E_0 J_1(\beta_1) e^{j[2\pi(f_{\mathrm{c}}+f_{\mathrm{s}})t-2\pi f_{\mathrm{c}}\upsilon t+\varphi_{\mathrm{c}}(t-\upsilon t)+\frac{\pi}{2}]} \\ &\quad + E_0 J_1(\beta_1) e^{j\left[2\pi(f_{\mathrm{c}}-f_{\mathrm{s}})t-2\pi f_{\mathrm{c}}\upsilon t+\varphi_{\mathrm{c}}(t-\upsilon t)+\frac{\pi}{2}\right]} \end{aligned} \tag{8}$$

where β_1 is the modulation index of PM1.

Then, two erbium-doped fiber amplifiers (EDFAs) are applied to boost the power of the optical signals in (7) and (8). Two optical bandpass filters (OBPFs) are followed to select out one of the first-order modulation sidebands, respectively, and suppress the amplified spontaneous emission noise. When the negative first-order sidebands are selected, the obtained optical signals after the two OBPFs are

$$E_3(t) \propto G_1 E_0 J_1(\beta_2) e^{j\left[2\pi(f_{\mathrm{c}}-f_{\mathrm{s}})(t-\upsilon t)+\varphi_{\mathrm{c}}(t-\upsilon t)+\frac{\pi}{2}\right]} \tag{9}$$

$$E_4(t) \propto G_2 E_0 J_1(\beta_1) e^{j\left[2\pi(f_{\mathrm{c}}-f_{\mathrm{s}})t-2\pi f_{\mathrm{c}}\upsilon t+\varphi_{\mathrm{c}}(t-\upsilon t)+\frac{\pi}{2}\right]} \tag{10}$$

where G_1 and G_2 are the gains of the two EDFAs. By comparing (9) and (10), it is found that the phase difference between $E_3(t)$ and $E_4(t)$ is "$2\pi f_{\mathrm{s}}\upsilon t$".

The optical signals in (9) and (10) are mixed in an optical 90° hybrid, followed by two BPDs to realize optical-to-electrical conversion. The voltages at the output of BPD1 and BPD2 are written as

$$\begin{aligned} v_{\mathrm{I}}(t) &\propto R_1 Z_L(\|E_3(t)+E_4(t)\|^2 - \|E_3(t)-E_4(t)\|^2) \\ &= 4Z_{\mathrm{L}}G_1G_2J_1(\beta_1)J_1(\beta_2)E_0^2R_1\cos(2\pi f_{\mathrm{s}}\upsilon t) \\ v_{\mathrm{Q}}(t) &\propto R_2 Z_L(\|E_3(t)+jE_4(t)\|^2 - \|E_3(t)-jE_4(t)\|^2) \\ &= 4Z_{\mathrm{L}}G_1G_2J_1(\beta_1)J_1(\beta_2)E_0^2R_2\sin(2\pi f_{\mathrm{s}}\upsilon t) \end{aligned} \tag{11}$$

where R_1 and R_2 are the responsivities of BPD1 and BPD2, respectively, and Z_L is the input impendence.

The electrical signals of $v_{\mathrm{I}}(t)$ and $v_{\mathrm{Q}}(t)$ are digitalized by a two-channel ADC, and the obtained digital signals are applied to calculate the frequency of the SUT by

$$\varphi(t) = 2\pi f_{\mathrm{s}}\upsilon t = \arctan\left(\frac{\frac{R_1}{R_2}v_{\mathrm{Q}}(t)}{v_{\mathrm{I}}(t)}\right) \tag{12}$$

$$f_{\mathrm{s}} = \frac{k[\varphi(t)]}{2\pi\upsilon}. \tag{13}$$

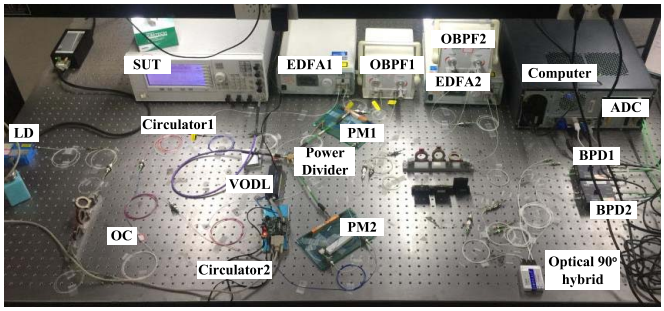

Fig. 3. Photograph of the experimental setup.

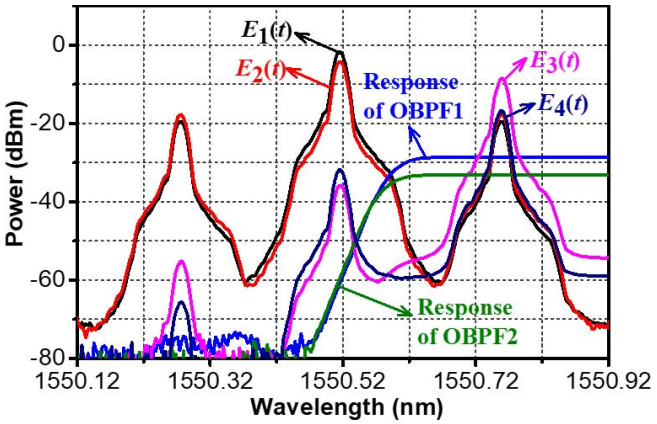

Fig. 4. Measured spectra of the optical signals $E_1(t)$, $E_2(t)$, $E_3(t)$, and $E_4(t)$, and responses of OBPF1 and OBPF2.

In (12), the ratio between the responsivities of the two BPDs (R_1/R_2) should be known before calculating the phase $\varphi(t)$. Based on (11), the maximum values of $v_{\mathrm{I}}(t)$ and $v_{\mathrm{Q}}(t)$ are proportional to R_1 and R_2, respectively, with the same coefficient. Thus, R_1/R_2 can be derived by

$$\frac{R_1}{R_2} = \frac{\max[v_{\mathrm{I}}(t)]}{\max[v_{\mathrm{Q}}(t)]}. \tag{14}$$

Equation (14) indicates that the calculation of R_1/R_2 can be implemented during the frequency measurement process using the same digital data, which can greatly simplify the frequency measurement procedure. It should be noted that the ratio R_1/R_2 can be treated as a constant for different frequencies under test, because the frequency of the electrical voltages output from the BPDs ($f_{\mathrm{s}}v$) changes a little compared with the bandwidth of the BPDs, even though the frequency under test (f_{s}) changes a lot.

III. Experimental Demonstration

To verify the feasibility of the proposed photonics-based IFM system, an experiment is conducted with the photograph of the setup shown in Fig. 3. Table I lists the main devices that are used in the experiment and their parameters. In the experiment, the sampling rate of the ADC is set to 20.48 kSa/s, and the varying speed of the VODL is set to 128 ps/s.

First of all, the frequency of the SUT is tuned to 30 GHz. Fig. 4 shows the spectra of the optical signals of $E_1(t)$ and $E_2(t)$, measured at the output of the fiber loop. In Fig. 4, spectra of the optical signals of $E_3(t)$ and $E_4(t)$ measured after the two OBPFs are also included. As can be seen, the undesired optical carriers and sidebands are suppressed by over 25 dB. At the output of the BPDs, a pair of I/Q voltages are acquired by the ADC. The waveforms of the two signals are plotted in Fig. 5(a). The I/Q waveforms are with almost equal amplitudes and a quadrature phase difference, indicating that the I/Q mixing is realized. Based on (12) and (14), a time-related phase term $\varphi(t)$ is calculated, as shown in Fig. 5(b).

To estimate the slope of the calculated phase with respect to time, a linear fitting based on the least-squares method is applied. Specifically, if the phases at time $t_1, t_2, \ldots, t_N$ are $\varphi_1, \varphi_1, \ldots, \varphi_N$, respectively, the phase slope with respect to time is estimated by

$$k = \frac{\frac{1}{N}\sum_{i=1}^{N} t_i\varphi_i - \frac{1}{N}\sum_{i=1}^{N} t_i \times \frac{1}{N}\sum_{i=1}^{N} \varphi_i}{\frac{1}{N}\sum_{i=1}^{N} t_i^2 - \left(\frac{1}{N}\sum_{i=1}^{N} t_i\right)^2}. \tag{15}$$

Fig. 6(a) shows the results for 100 consecutive estimations of the phase slope when the input frequency is set to 30 GHz. In obtaining these results, the value of N in (15) is chosen to be 10. According to (13), the frequency of the SUT can be derived. Fig. 6(b) shows the measured frequencies corresponding to the phase slope in Fig. 6(a). The average value

TABLE I
Main Devices in the Experimental Setup

Device	Manufacturer, Version	Parameters
LD	TeraXion, PS-NLL-1550.52-080-000-A1	Wavelength: 1550.52 nm; Output Power: 19 dBm
SUT	Agilent, E8257D-option 567	Tunable range: 250 kHz-67 GHz
VODL	General Photonics, VDL-001-15-600-SM-FC/APC	Range of time delay: 0-330 ps Varying speed: 0.01-256 ps/s (10 discrete speeds) Control mode: RS-232 interface
PM1,2	EOSPACE, PM-DV5-40-PFA-PFA-LV	3-dB bandwidth*: 40 GHz
EDFA1,2	Amonics, AEDFA-35-B-FA	Gain: >35 dB (input power < -10 dBm)
OBPF1,2	Yenista, XTM-50/S	Tuning range: 1450-1650 nm; Bandwidth: 50-950 pm; Edge roll-off: 500 dB/nm
Optical 90° hybrid	Kylia, COH28	Operating wavelength: 1520-1570 nm Phase shift between I and Q: 85°-95°
BPD1,2	Thorlabs, PDB450C	3-dB bandwidth: 150 MHz; Responsivity: 0.53 A/W Transimpedance gain: 10^3 V/A
ADC	National Instruments, PCI-4462	Maximum sampling rate: 204.8 kSa/s; Number of channels: 4; Sampling resolution: 24 bit
Power divider	Malaysia	Bandwidth: 0-50 GHz

* The PMs can be used for phase modulation at frequencies beyond the 3-dB bandwidth with reduced electro-optic modulation response.

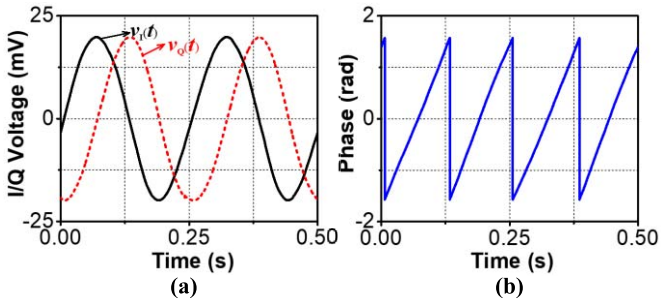

Fig. 5. (a) Waveforms of the signals corresponding to I and Q channels. (b) Calculated time-varying phase.

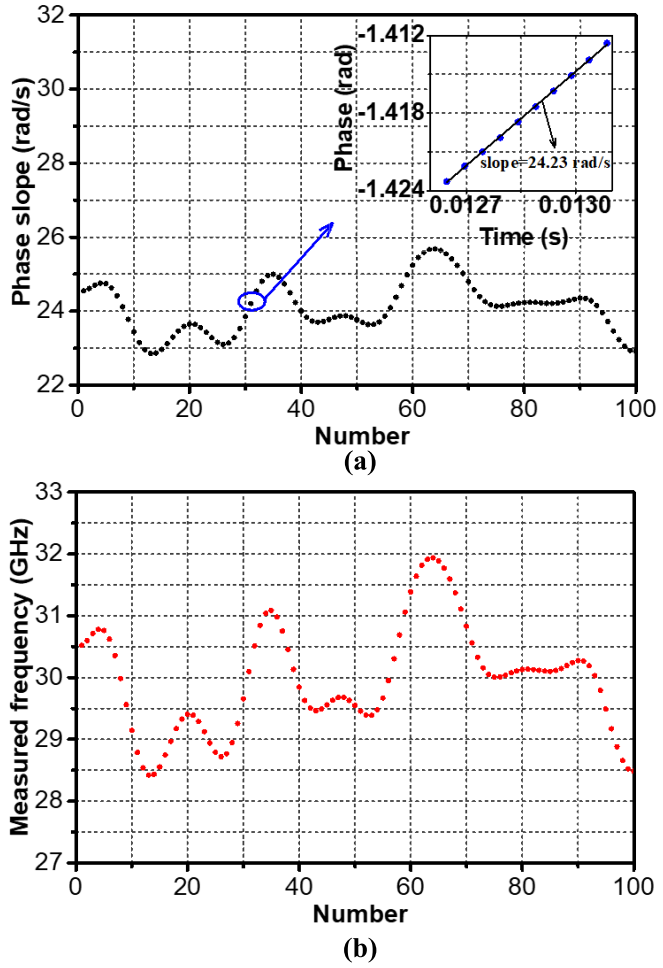

Fig. 6. 100 consecutive estimation results of (a) slope of the calculated phase with respect to time (Inset: example of estimating the slope from 10 phase points using linear fitting algorithm) and (b) estimated frequency according to the estimated slope.

of the 100 estimated frequencies in Fig. 6(b) is 29.955 GHz, and the average measurement error is 45 MHz.

It should be noted that the time for a single measurement is $T_s = N/F_s$, where F_s is the sampling rate of the ADC. In this experiment, $N = 10$ and $F_s = 20.48$ kSa/s, the time for a single measurement is approximately 0.49 ms. This measurement time corresponds to an updating rate larger than 2 kHz,

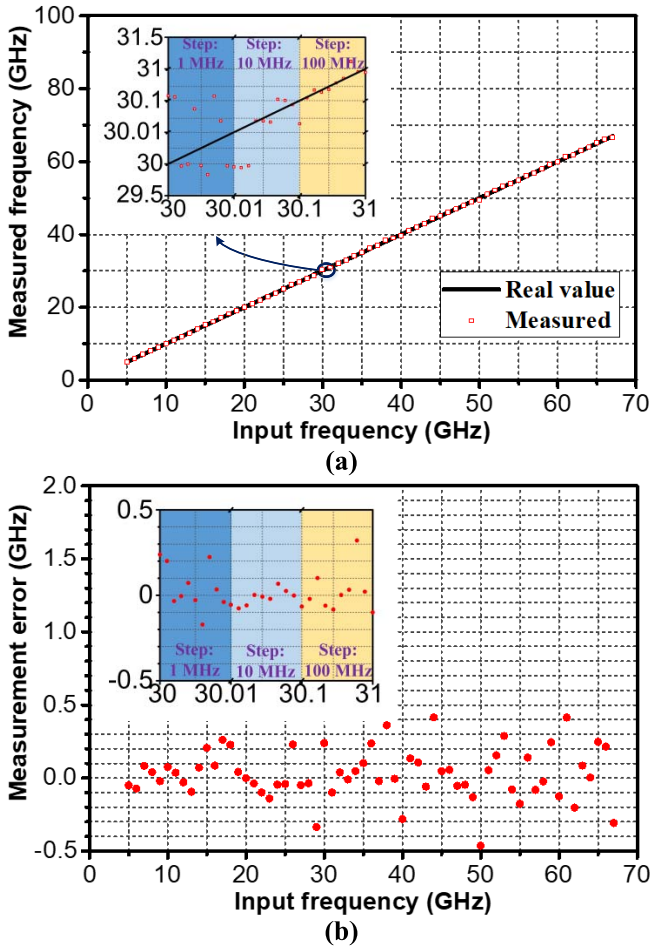

Fig. 7. (a) Measured frequencies and (b) measurement errors versus input frequencies from 5 to 67 GHz. Insets: measured frequencies and errors versus input frequency tuned from 30 to 31 GHz with different steps.

indicating a very fast frequency measurement is achieved. Here, the frequency measurement time can be further reduced by increasing the sampling rate of the ADC and/or choosing a smaller N. The time required for obtaining the averaged frequency estimation is related to the sampling rate (F_s), the value of N, and the times of measurements (Num) by $T_m = (\text{Num} + N - 1)/F_s$, where $\text{Num} + N - 1$ represents the length of time sequence required for Num times consecutive measurements. In the experiment, the total measurement time for 100× consecutive measurements is approximately 5 ms.

Then, to demonstrate the wide frequency measurement range of the proposed IFM system, the frequency of the SUT is tuned from 5 to 67 GHz with a step of 1 GHz. The measurement process is the same with the processing in obtaining the results in Fig. 6, i.e., the averaged value of 100 consecutive frequency estimations is used as the output of the IFM system. Fig. 7(a) shows the measured frequencies corresponding to different input frequencies from 5 to 67 GHz with a step of 1 GHz. The measurement errors at different frequencies are plotted in Fig. 7(b), which are kept within ±500 MHz in the whole frequency range from 5 to 67 GHz. It should be noted that, when a smaller frequency step is

TABLE II
PERFORMANCE COMPARISON BETWEEN THE PROPOSED IFM SYSTEM AND THE PREVIOUSLY REPORTED SYSTEMS

	Measurement range (GHz)	Measurement error (GHz)	Applicability to multi-tone signals
This work	5-67	±0.5	No
Ref. [9]	15-45	±1.56	Yes
Ref. [10]	0.1-20	±0.25	Yes
Ref. [11]	1-23	NA	Yes
Ref. [12]	1-18	±1	Yes
Ref. [15]	4-12	±0.1	No
Ref. [16]	4-19	±0.1	No
Ref. [17]	5-15.6	±0.1	No
Ref. [18]	0-12.7	±0.2	No
Ref. [19]	0-12	±0.25	No
Ref. [20]	1-26	±0.2	No
Ref. [21]	1-20	±0.2	No
Ref. [22]	2-19	±0.2	No
Ref. [23]	1-10	±0.08	No
Ref. [24]	0.5-36	±0.2	No

chosen, the measurement errors are at the same level. The insets of Fig. 7 show the measurement results with a step of 1, 10, and 100 MHz for the frequency ranges of 30–30.01, 30.01–30.1, and 30.1–31 GHz, respectively, where the measurement errors are also kept within ±500 MHz. In this demonstration, the lower limit of the frequency measurement range is limited to 5 GHz due to the edge slope of the tunable OBPFs, which should be sharp enough to separate the first-order sideband from the optical carrier [30].

Compared with the previously reported IFM systems, the proposed IFM system has several advantages. First, the systems in [9] and [10] that make use of frequency-to-time mapping suffer from bandwidth limitation by the speed of the optical ON–OFF switching and the sampling rate of the oscilloscope [9], or the measurement time [10], while the proposed IFM system is free from high-speed electrical components and high-sampling-rate oscillators (ADC), which helps to achieve a broad operating bandwidth. Second, compared with the systems in [11] and [12] that apply frequency-to-space mapping, the proposed system is significantly simplified and economical. Finally, a common problem for the frequency-to-power mapping-based systems [15]–[24] is the frequency measurement ambiguity due to the nonmonotonic mapping, which limits the unambiguous frequency measurement range. Another disadvantage of the frequency-to-power mapping-based systems is difficult to perform high-resolution measurement for some frequencies due to the small slope of ACF at these frequencies. Different from the frequency-to-power mapping, the proposed frequency-to-phase-slope mapping is monotonic and linear, indicating the proposed system is free from measurement ambiguity and imprecise measurements for some specific frequencies. Table II lists a comparison between the proposed IFM system and previously reported photonics-based IFM systems, where the measurement range, the measurement error, and the applicability to multitone signals are considered. It can be seen from the results in Table II, the proposed IFM system has a recorded frequency measurement range that can be achieved by photonics-based IFM systems. However, the proposed frequency-to-phase-slope mapping method is not suitable for measuring multitone microwave signals.

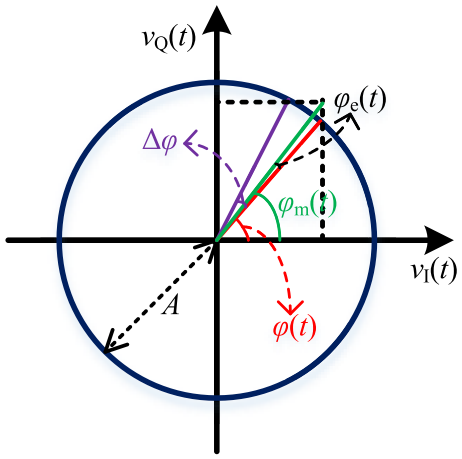

Fig. 8. Diagram for analyzing the influence of phase mismatch between I/Q voltages.

IV. DISCUSSION

In the description of the operation principle, the I/Q mixer is assumed to have an ideal quadrature phase difference between I and Q channels. In practice, the nonideal performance of the devices could easily cause phase mismatch between I and Q channels, which would result in the frequency measurement errors. In addition, the amplitude noise in the acquired I/Q voltages due to the active devices (such as the BPDs and the ADC) would also affect the frequency measurement accuracy. In this section, the effects of the I/Q phase mismatch and the amplitude noise on the IFM system are analyzed.

A. I/Q Phase Mismatch Analysis

Assuming that the phase mismatch between I and Q channels is $\Delta\varphi$, the I/Q voltages acquired by the ADC can be written as

$$\begin{aligned} v_I(t) &\propto A\cos(\varphi(t)) \\ v_Q(t) &\propto A\sin(\varphi(t)+\Delta\varphi) \end{aligned} \tag{16}$$

where $\varphi(t) = 2\pi f_s\, vt$. Due to the phase mismatch, the calculated phase is not equal to $\varphi(t)$ anymore. According to Fig. 8, the phase when the phase mismatch exists can be calculated by

$$\begin{aligned} \varphi_m(t) &= \varphi(t) + \varphi_e(t) \\ &\approx \varphi(t) + \frac{A\sin(\varphi(t)+\Delta\varphi) - A\sin(\varphi(t))}{A} \\ &\approx \varphi(t) + \Delta\varphi\cos(\varphi(t)). \end{aligned} \tag{17}$$

Accordingly, the slope of $\varphi_m(t)$ with respect to time is

$$k_m(t) = \frac{d\varphi_m(t)}{dt} = 2\pi f_s v - \Delta\varphi 2\pi f_s v\sin(2\pi f_s vt). \tag{18}$$

As a result, the measured frequency is

$$f_m = \frac{k_m(t)}{2\pi v} = f_s - \Delta\varphi f_s\sin(2\pi f_s vt). \tag{19}$$

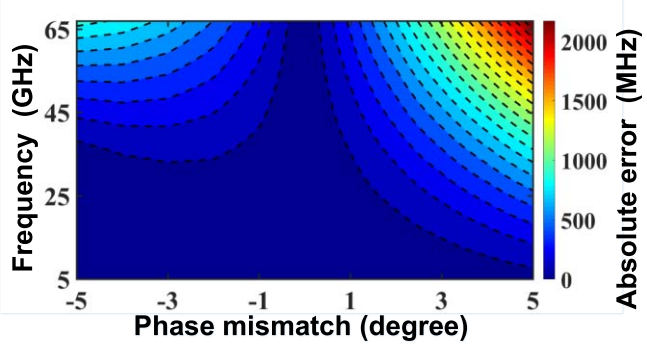

Fig. 9. Simulation results of the frequency measurement error corresponding to different phase mismatches and frequencies.

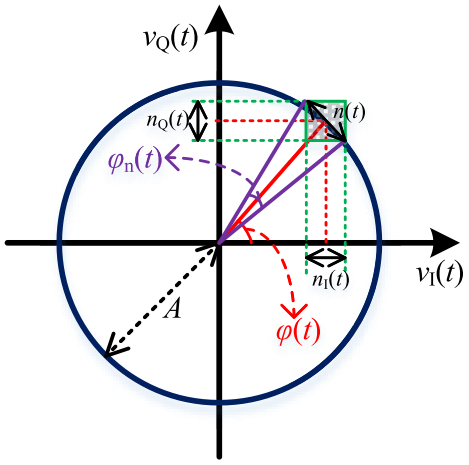

Fig. 10. Diagram for analyzing the influence of amplitude noise in I/Q voltages.

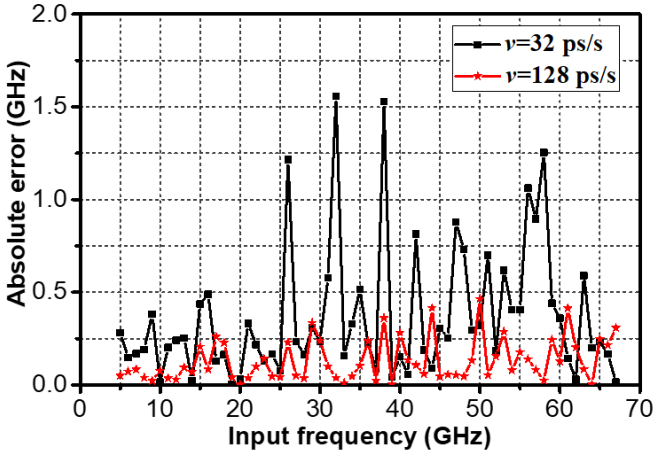

Fig. 11. Frequency measurement error versus input frequency when the varying speeds are set to 32 and 128 ps/s, respectively.

It can be seen that the frequency measurement error is related to the phase mismatch ($\Delta\varphi$) and the frequency to be measured (f_s). With the increase of phase mismatch or frequency to be measured, the error increases.

In the proposed photonics-based IFM system, the phase mismatch is mainly due to the nonideal quadrature phase property of the optical 90° hybrid and the path length difference of between I and Q channels. In fact, the phase mismatch can be easily compensated in the DSP unit, as demonstrated in [31]. Although the phase mismatch problem is not the main concern in our experiment, a simulation is carried out to show the influence of the phase mismatch clearly. In the simulation, the parameters are chosen according to the previous experimental demonstration, i.e., the varying speed of the time delay is 128 ps/s, and the time sequence with 109 points starts from 0 with a sampling rate of 20.48 kSa/s. Fig. 9 shows the frequency measurement error when the phase mismatch changes from −5° to 5° with a step of 1°, and the frequency to be measured changes from 5 to 67 GHz with a step of 1 GHz. It can be seen that a larger measurement error occurs as the increase of the phase mismatch and/or the frequency of the SUT, which agrees well with (19).

B. Amplitude Noise Analysis

Assuming that the amplitude noises in I and Q channels [$n_I(t)$ and $n_Q(t)$] are unrelated additive noise with the same distribution. The effect of the amplitude noise is depicted in Fig. 10, where the additive noise introduces a phase fluctuation $\varphi_n(t)$ to phase $\varphi(t)$. When $n(t)$ is far less than A, the calculated phase can be written as

$$\varphi_o(t) = \varphi(t) + \varphi_n(t) \tag{20}$$

$$\approx \varphi(t) + \frac{\sqrt{|n_I(t)|^2 + |n_Q(t)|^2}}{A}$$

$$= \varphi(t) + \frac{n(t)}{A} \tag{21}$$

$$n(t) \ll A. \tag{22}$$

The slope of $\varphi_o(t)$ with respect to time is

$$k_o(t) = \frac{d\varphi_o(t)}{dt} = 2\pi f_s v + \frac{dn(t)}{Adt}. \tag{23}$$

Accordingly, the estimated frequency is

$$f_o = \frac{k_o(t)}{2\pi v} = f_s + \frac{1}{2\pi v A}\frac{dn(t)}{dt}. \tag{24}$$

It can be seen that the measurement error is not only dependent on the noise but also related to the varying speed of the time delay introduced by the VODL.

According to (22), a larger varying speed of the time delay can help to archive a smaller measurement error. To show this property, an experiment is performed, in which the frequency of the SUT is tuned from 5 to 67 GHz with a step of 1 GHz. Fig. 11 shows the frequency measurement errors when the varying speed of the time delay is set to 32 and 128 ps/s, respectively. In Fig. 11, the measurement errors are significantly reduced by choosing a large varying speed of the time delay. Thus, it is highly desirable to employ a fast varying time delay in this method. However, this would put forward higher requirement of the VDL.

V. Conclusion

We have proposed a new IFM method based on the frequency-to-phase-slope mapping, in which the frequency is monotonously mapped to the phase slope of the SUT. Thanks to the monotony of the frequency-to-phase-slope mapping, the frequency measurement is free from measurement ambiguity. Based on this principle, a photonics-based IFM system utilizing a VODL and a microwave photonic I/Q mixer is proposed and experimentally demonstrated. Thanks to the unambiguous frequency measurement property, this photonics-based IFM system can achieve a large operation bandwidth by applying a broadband VODL and microwave photonic I/Q mixer. In the experiment, a record frequency measurement range from 5 to 67 GHz is demonstrated with an average measurement error of less than 500 MHz. At last, the effects of the I/Q phase mismatch and the amplitude noise on the frequency measurement performance are investigated.

References

[1] R. G. Wiley, *Electronic Intelligence: The Analysis of Radar Signals*. Boston, MA, USA: Artech House, 1993.

[2] A. E. Spezio, "Electronic warfare systems," *IEEE Trans. Microw. Theory Techn.*, vol. 50, no. 3, pp. 633–644, Mar. 2002.

[3] F. Scotti, F. Laghezza, P. Ghelfi, and A. Bogoni, "Multi-band software-defined coherent radar based on a single photonic transceiver," *IEEE Trans. Microw. Theory Techn.*, vol. 63, no. 2, pp. 546–552, Feb. 2015.

[4] F. Z. Zhang, "Photonics-based broadband radar for high-resolution and real-time inverse synthetic aperture imaging," *Opt. Express*, vol. 25, no. 14, pp. 16274–16281, Jul. 2017.

[5] P. W. East, "Fifty years of instantaneous frequency measurement," *IET Radar Sonar Navigat.*, vol. 6, no. 2, pp. 112–122, Feb. 2012.

[6] J. Yao, "Microwave photonics," *J. Lightw. Technol.*, vol. 27, no. 3, pp. 314–335, Feb. 1, 2009.

[7] S. L. Pan and J. P. Yao, "Photonics-based broadband microwave measurement," *J. Lightw. Technol.*, vol. 35, no. 16, pp. 3498–3513, Aug. 15, 2017.

[8] X. Zou, B. Lu, W. Pan, L. S. Yan, A. Stöhr, and J. P. Yao, "Photonics for microwave measurements," *Laser Photon. Rev.*, vol. 10, no. 5, pp. 711–734, Sep. 2016.

[9] L. V. T. Nguyen, "Microwave photonic technique for frequency measurement of simultaneous signals," *IEEE Photon. Technol. Lett.*, vol. 21, no. 10, pp. 642–644, May 15, 2009.

[10] T. A. Nguyen, E. H. W. Chan, and R. A. Minasian, "Instantaneous high-resolution multiple-frequency measurement system based on frequency-to-time mapping technique," *Opt. Lett.*, vol. 39, no. 8, pp. 2419–2422, Mar. 2014.

[11] S. T. Winnall, A. C. Lindsay, M. W. Austin, J. Canning, and A. Mitchell, "A microwave channelizer and spectroscope based on an integrated optical Bragg-grating Fabry–Perot and integrated hybrid Fresnel lens system," *IEEE Trans. Microw. Theory Techn.*, vol. 54, no. 2, pp. 868–872, Feb. 2006.

[12] L. X. Wang, N. H. Zhu, W. Li, H. Wang, J. Y. Zheng, and J. G. Liu, "Polarization division multiplexed photonic radio-frequency channelizer using an optical comb," *Opt. Commun.*, vol. 286, pp. 282–287, Jan. 2013.

[13] J. M. Heaton, "16-channel (1- to 16-GHz) microwave spectrum analyzer device based on a phased array of GaAs/AlGaAs electro-optic waveguide delay lines," *Proc. SPIE*, vol. 3278, pp. 245–251, Jan. 1998.

[14] W. S. Wang, "Characterization of a coherent optical RF channelizer based on a diffraction grating," *IEEE Trans. Microw. Theory Techn.*, vol. 49, no. 10, pp. 1996–2001, Oct. 2001.

[15] L. V. T. Nguyen and D. B. Hunter, "A photonic technique for microwave frequency measurement," *IEEE Photon. Technol. Lett.*, vol. 18, no. 10, pp. 1188–1190, May 2006.

[16] M. Attygalle and D. B. Hunter, "Improved photonic technique for broadband radio-frequency measurement," *IEEE Photon. Technol. Lett.*, vol. 21, no. 4, pp. 206–208, Feb. 15, 2009.

[17] X. Zou and J. Yao, "An optical approach to microwave frequency measurement with adjustable measurement range and resolution," *IEEE Photon. Technol. Lett.*, vol. 20, no. 23, pp. 1989–1991, Dec. 1, 2008.

[18] J. Li, "Photonic-assisted microwave frequency measurement with higher resolution and tunable range," *Opt. Lett.*, vol. 34, no. 6, pp. 743–745, Mar. 2009.

[19] W. Li, N. H. Zhu, and L. X. Wang, "Brillouin-assisted microwave frequency measurement with adjustable measurement range and resolution," *Opt. Lett.*, vol. 37, no. 2, pp. 166–168, Jan. 2012.

[20] X. H. Zou, H. Chi, and J. P. Yao, "Microwave frequency measurement based on optical power monitoring using a complementary optical filter pair," *IEEE Trans. Microw. Theory Techn.*, vol. 57, no. 2, pp. 505–511, Feb. 2009.

[21] H. Chi, X. Zou, and J. Yao, "An approach to the measurement of microwave frequency based on optical power monitoring," *IEEE Photon. Technol. Lett.*, vol. 20, no. 14, pp. 1249–1251, Jul. 15, 2008.

[22] X. Zou, S. Pan, and J. Yao, "Instantaneous microwave frequency measurement with improved measurement range and resolution based on simultaneous phase modulation and intensity modulation," *J. Lightw. Technol.*, vol. 27, no. 23, pp. 5314–5320, Dec. 1, 2009.

[23] Z. Li, B. Yang, H. Chi, X. Zhang, S. Zheng, and X. Jin, "Photonic instantaneous measurement of microwave frequency using fiber Bragg grating," *Opt. Commun.*, vol. 283, no. 3, pp. 396–399, Feb. 2010.

[24] S. Pan and J. Yao, "Instantaneous microwave frequency measurement using a photonic microwave filter pair," *IEEE Photon. Technol. Lett.*, vol. 22, no. 19, pp. 1437–1439, Oct. 1, 2010.

[25] F. Z. Zhang, J. Z. Shi, and S. L. Pan, "Photonics-based wideband Doppler frequency shift measurement by in-phase and quadrature detection," *Electron. Lett.*, vol. 54, no. 11, pp. 708–710, May 2018.

[26] J. Z. Shi, F. Z. Zhang, D. Ben, and S. L. Pan, "Wideband microwave phase noise analyzer based on an ll-optical microwave I/Q amixer," *J. Lightw. Technol.*, vol. 36, no. 19, pp. 4319–4325, Oct. 1, 2018.

[27] J. Z. Shi, F. Z. Zhang, D. Ben, and S. L. Pan, "Wideband microwave photonic I/Q mixer based on parallel installed phase modulator and Mach-Zehnder modulator," in *Proc. IEEE Int. Wireless Symp. (IWS)* Chengdu, China, May 2018, pp. 1–4.

[28] Z. Z. Tang and S. L. Pan, "A reconfigurable photonic microwave mixer using a 90° optical hybrid," *IEEE Trans. Microw. Theory Techn.*, vol. 64, no. 9, pp. 3017–3025, Sep. 2016.

[29] K. Jung and J. Kim, "Subfemtosecond synchronization of microwave oscillators with mode-locked Er-fiber lasers," *Opt. Lett.*, vol. 37, no. 14, pp. 2958–2960, Jul. 2012.

[30] F. Zhang, J. Shi, and S. Pan, "Wideband microwave phase noise measurement based on photonic-assisted I/Q mixing and digital phase demodulation," *Opt. Express*, vol. 25, no. 19, pp. 22760–22768, Sep. 2017.

[31] J. Z. Shi, F. Z. Zhang, and S. L. Pan, "Phase noise measurement of RF signals by photonic time delay and digital phase demodulation," *IEEE Trans. Microw. Theory Techn.*, vol. 66, no. 9, pp. 4306–4315, Sep. 2018.

Jingzhan Shi received the B.S. and M.S. degrees in electronic and information engineering from the Nanjing University of Aeronautics and Astronautics, Nanjing, China, in 2013 and 2016, respectively, where he is currently pursuing the Ph.D. degree at the Key Laboratory of Radar Imaging and Microwave Photonics, Ministry of Education.

His current research interests include photonics-assisted analysis of microwave signals.

Fangzheng Zhang (S'10–M'13) received the B.S. degree from the Huazhong University of Science and Technology, Wuhan, China, in 2008, and the Ph.D. degree from the Beijing University of Posts and Telecommunications, Beijing, China, in 2013.

He is currently an Associate Professor with the College of Electronic and Information Engineering, Nanjing University of Aeronautics and Astronautics, Nanjing, China. His current research interests include microwave photonics and optical communications.

De Ben, photograph and biography are not available at the time of publication.

Shilong Pan (S'06–M'09–SM'13) received the B.S. and Ph.D. degrees in electronics engineering from Tsinghua University, Beijing, China, in 2004 and 2008, respectively.

From 2008 to 2010, he was a "Vision 2010" Post-Doctoral Research Fellow with the Microwave Photonics Research Laboratory, University of Ottawa, Ottawa, ON, Canada. In 2010, he joined the College of Electronic and Information Engineering, Nanjing University of Aeronautics and Astronautics, Nanjing, China, where he is currently a Full Professor and the Deputy Director of the Key Laboratory of Radar Imaging and Microwave Photonics, Ministry of Education.

He has authored or co-authored over 380 research papers, 200 papers in peer-reviewed journals, and 180 papers in conference proceedings. His current research interests include microwave photonics, which includes the optical generation and processing of microwave signals, analog photonic links, photonic microwave measurement, and integrated microwave photonics.

Prof. Pan is a Fellow of the IET and a Senior Member of the OSA and SPIE. He was a recipient of the OSA Outstanding Reviewer Award in 2015, a Top Reviewer of the IEEE/OSA JOURNAL OF LIGHTWAVE TECHNOLOGY in 2016, the Excellent Young Scholars Award of the National Natural Science Foundation of China in 2014, and the Scientific and Technological Innovation Leading Talents Award of the National Ten Thousand Plan in 2018. He is currently a Topical Editor of *Chinese Optics Letters* and a Technical Committee member of IEEE MTT-3 Microwave Photonics. He is a Steering Committee member of the IEEE International Topical Meeting on Microwave Photonics and International Conference on Optical Communications and Networks. He has also served as the Chair for a number of international conferences, symposia, and workshops, including the TPC Chair for the International Conference on Optical Communications and Networks in 2015, a TPC Co-Chair for the IEEE International Topical Meeting on Microwave Photonics in 2017, the TPC Subcommittee Chair or a Co-Chair for the IEEE Radio Wireless Symposium in 2013, 2014, and 2016, the OptoElectronics and Communication Conference in 2015, the CLEO Pacific Rim in 2018, the International Conference on Information Optics and Photonics in 2018, and the Chair for the Microwave Photonics for Broadband Measurement Workshop of the IEEE MTT-S International Microwave Symposium in 2015.